Article

Redox-Mediated Reversible Supramolecular Assemblies Driven by Switch and Interplay of Peptide Secondary Structures

Qingxin Yao,[||] Guangqi Wu,[||] Hao Hao,[||] Hua Lu,* and Yuan Gao*

Read Online

ACCESS | Metrics & More | Article Recommendations | SI Supporting Information

ABSTRACT: The construction of reversible supramolecular self-assembly *in vivo* remains a significant challenge. Here, we demonstrate the redox-triggered reversible supramolecular self-assembly governed by the "check and balance" of two secondary conformations within a brushlike peptide−selenopolypeptide conjugate. The conjugate constitutes a polypeptide backbone whose side chain contains selenoether functional moieties and double bonds to be readily grafted with β-sheet-prone short-peptide NapFFC. The backbone of the conjugate initially assumes a robust and rigid α-helical conformation, which inhibits the supramolecular assembly of the short peptide in the side chain and yields an overall irregular aggregate morphology under native/reduced conditions. Upon oxidation of the selenoether to more hydrophilic selenoxide, the backbone helix switches to a flexible and disordered conformation, which unleashes the side-chain NapFFC self-assembly into nanofibrils via the adoption of β-sheet conformation. The reversible switch of the supramolecular morphology enables efficient loading and tumor-microenvironment-triggered release of anticancer drugs for *in vivo* cancer treatment with satisfactory efficacy and biocompatibility. The interplay and interaction between two well-defined secondary structures within one scaffold offer tremendous opportunity for the design and construction of functional supramolecular biomaterials.
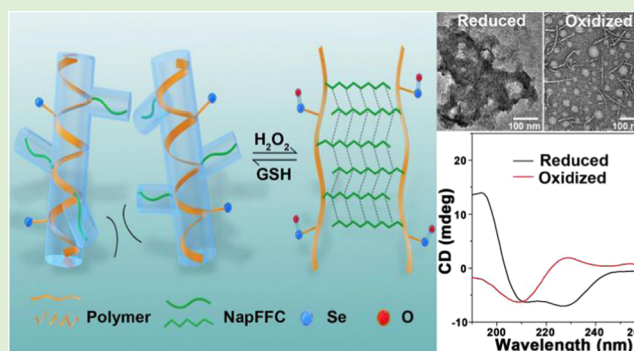
1. INTRODUCTION

Living organisms are orchestrated collections of hierarchical supramolecular assemblies including the phospholipid bilayer membrane, cytoskeleton, and double-strand DNA to name a few.[1,2] Often, these assemblies share the common key feature of dynamic assembly—disassembly processes to support cell division, achieve adaptive correspondence, and realize complex functions.[3,4] The bioinspired stimuli-responsive dynamic structural changes have already elicited fruitful outcomes in the design of functional synthetic biomaterials in biotechnology and nanomedicine.[5] These smart biomaterials function via either bottom-up construction or top-down destruction[6] under the external or internal stimuli such as light,[7] magnetic field,[8] electric field,[9] ultrasound,[10] pH,[11,12] metal ions,[13] temperature,[14] carbon dioxide,[15] redox,[16] enzyme,[5] DNA,[17,18] etc.

Polypeptides prepared by the ring-opening polymerization (ROP) of *N*-carboxyanhydride (NCA) are fascinating biomimetic and biomedical materials with stimuli-responsibility, biodegradability, and additional attractive functionalities.[19−21] The intra- and inter-molecular hydrogen bonds render polypeptides with unique protein-like secondary structures, making it a favorable candidate for supramolecular assembly.[22] For example, amphiphilic block copolypeptides with helical hydrophobic blocks showed more tendency to form hydrogels.[23] Decades of research revealed that many synthetic polypeptides could undergo reversible secondary structure change (e.g., helix-to-coil transition) under an external stimulus.[13,24−31] The precise conformational control provides a possibility for developing versatile peptide-based biomaterials, offering potential applications in drug delivery, biosensing, and tissue engineering.[32−38]

Among many triggers exploited, redox represents an intriguing class for its biorelevance and implication related to many pathological processes such as inflammation and cancer. Thioether-containing polypeptide is one of the promising candidates to respond to the signal.[39] Deming *et al.* have shown that many polypeptides with thioether groups performed a redox-responsive conformational transition.[27,40,41] Recently, Ding *et al.* demonstrated the oxidation-induced thioether-to-sulfone conversion of a cholesterol-containing polypeptide, which led to the β-sheet to α-helix conformation change and, consequently, a micelle-to-vesicle transition of the self-assembled morphology.[42] Such materials hold promise for drug delivery, tissue engineering, and immunotherapy.[43,44]

However, the oxidation of thioether was kinetically slow and the reversed process required enzymatic catalysis under biorelevant conditions.[45] The redox-triggered selenoether−selenoxide conversion, on the contrary, can be realized under much milder and more biofriendly conditions in both directions.[46−49] For this, we have recently introduced selenoether to the side chain of polypeptides. The selenopolypeptide showed α-helical conformation in the native state and it could undergo a reversible helix-to-coil transition in response to redox signals.[50] Despite these advancements, there are very few studies demonstrating reversible transition between two ordered secondary structures, not to mention the successive regulation of the hierarchical self-assembly by such a conformation switch.

Here, we report a sustained redox-regulated reversible self-assembly that is delicately controlled by the interaction and interplay of two different structural units that existed within a brushlike selenopolypeptide. The selenopolypeptide, namely, pSe-NapFFC-Glu, bears two different functional moieties in its side chain: one is the redox-sensitive selenoether and the other is a short-peptide NapFFC which could undergo supramolecular assembly. The backbone initially adopts the α-helical conformation. We hypothesize that the "check and balance" of the backbone α-helix and the side chain β-sheet peptide dictates the self-assembly of the brushlike polypeptide, which can be reversibly controlled by the oxidation states of the selenoether groups in the side chain (Scheme 1). Briefly,

Scheme 1. Schematic Illustration of Redox-Regulated Reversible Supramolecular Assemblies via Conformation Switch of Brushlike Selenopolypeptides
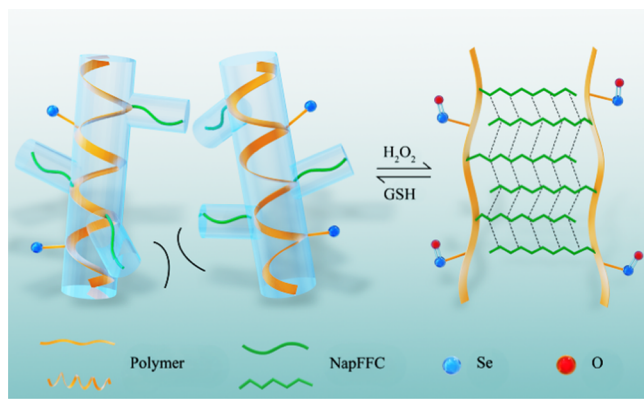
under native/reduced conditions, the rigid helical backbone would minimize the stacking of the side chain peptide, rendering irregular self-assemblies/aggregates. After oxidation, the selenoxide would lead to a more flexible backbone structure owing to the helix-to-coil transition, which could consequently unleash NapFFC self-assembling into β-sheet and even higher ordered architectures. Upon micellization of pSe-NapFFC-Glu, these order-to-order redox reversible assemblies are readily applicable for sensing oxidative stress and drug delivery. This redox responsive biomaterial showed outstanding anticancer efficacy with satisfactory biosafety in a mouse tumor model.

2. MATERIALS AND METHODS

2.1. Materials and Instruments. All chemical reagents were used as received from commercial sources. NMR spectra were recorded on a Bruker 400 MHz Fourier transform spectrometer. Transmission

electron microscopy (TEM) images were obtained on a Tecnai G2 20 S-TWIN transmission electron microscope. Circular dichroism (CD) UV spectra were recorded on a Jasco J-1500 CD spectrometer. The fluorescence intensity was measured on an EnSpire multimode plate reader from PerkinElmer.

2.2. Synthesis of the Short Peptide. The peptide was synthesized via solid-phase peptide synthesis (SPPS) using 2-chlorotrity resin and the corresponding Fmoc-protected amino acids. The synthesis route and molecular structures of NapFFC and CFFY are shown in Figures S1 and S2, respectively. ^{1}H NMR spectra of NaFFC and CFFY are shown in Figures S3 and S4, respectively.

^{1}H NMR of NaFFC (DMSO-d_6, 400 MHz) δ (ppm): 13.16−12.72 (s, 1H), 8.33−8.20 (m, 3H), 7.87−7.82 (d, 1H), 7.81−7.72 (m, 2H), 7.60−7.56 (s, 1H), 7.51−7.42 (m, 2H), 7.29−7.09 (m, 11H), 4.66−4.57 (m, 1H), 4.57−4.49 (m, 1H), 4.49−4.41 (m 1H), 3.62−3.45 (q, 2H), 3.11−3.02 (q,1H), 3.02−2.93 (q,1H), 2.93−2.67 (m, 4H), 2.46−2.39 (t, 1H) (Figure S3).

ESI/MS (m/z): calcd for $C_{33}H_{33}N_3O_5S$, 583.21; found $[M + H]^+$, 584.30.

^{1}H NMR of CFFY (DMSO-d_6, 400 MHz) δ (ppm): 8.48−8.40 (d, 1H), 8.36−8.23 (q, 2H), 7.27−7.05 (m, 10H), 7.02−6.93 (d, 2H), 6.66−6.56 (d, 2H), 4.62−4.47 (m, 2H), 4.38−4.29 (m, 1H), 3.85−3.76 (m, 1H), 3.04−2.83 (m,3H), 2.83−2.63 (m, 3H) (Figure S4).

ESI/MS (m/z): calcd for $C_{30}H_{34}N_4O_6S$, 578.22; found $[M + H]^+$, 579.10.

2.3. Synthesis of NCA. Preparation of EG$_4$-SeHC NCA and EG$_3$ene-Glu NCA was carried out as previously reported.[25,50]

2.4. Ring-Opening Polymerization of NCA. Polymerization was carried out in a glovebox filled with ultrapure nitrogen. To a solution of EG$_4$-SeHC NCA (200 mg, 0.5 mmol) and EG$_3$ene-Glu NCA (116 mg, 0.33 mmol) in 2 mL of dry dimethylformamide (DMF), 160 μL of 0.1 M benzylamine DMF solution was quickly added. The reaction mixture was stirred at room temperature for 24 h, and the polymerization process was monitored by Fourier transform infrared (FTIR) spectroscopy. After the completion of the reaction, the polypeptides were precipitated and washed with diethyl ether. The products were then dissolved in water and lyophilized. The polypeptide was obtained as white sticky gums (214 mg, yield 77%).

2.5. Characterization of Selenopolypeptides by Size Exclusion Chromatography (SEC). Size exclusion chromatography (SEC) experiments were performed on a system equipped with an isocratic pump (Model 1100, Agilent Technology, Santa Clara, CA), a DAWN HELEOS 9-angle laser light scattering detector (MALLS, Wyatt Technology, Santa Barbara, CA), and an Optilab rEX refractive index detector (Wyatt Technology, Santa Barbara, CA). The detection wavelength of MALLS was 658 nm, and the temperature of both the refractive index and MALLS detectors was 25 °C. Separations were performed by serially connected size exclusion columns (500, 103, 104, and 105 Å Phenogel columns, 5 μm, 7.8 mm × 300 mm, Phenomenex, Torrance, CA) at a flow rate of 1.0 mL/min and 50 °C using DMF containing 0.1 M LiBr as the mobile phase (Figure S5).

2.6. General Procedure for the Synthesis of Brushlike Selenopolypeptides. pSe-Glu (100 mg) was dissolved in 5 mL of DMF followed by the addition of 35 mg of peptide NapFFC and 10 mg of benzoin dimethyl ether (2,2-dimethoxy-2-phenylacetophenone, DMPA). The system was radiated under UV for 1 h. The reaction was purified by dialysis (molecular weight cutoff, MWCO, 7 kDa) at 4 °C against carbonate−bicarbonate buffer (0.1 M, pH 10) for 48 h, followed by deionized water for another 24 h with water changing every 8 h. The product was obtained as a light yellow fluffy powder after lyophilization (130 mg, yield: 96%).

Other brush polymers were synthesized by following a similar procedure with the variance of the feeding ratio.

2.7. Oxidation and Reduction of the Brushlike Selenopolypeptides. The selenopolypeptide (1.0 mg/mL in water) was treated with 97 mM H$_2$O$_2$ for oxidation or 120 mM glutathione (GSH) for reduction. After each treatment, the sample was filtered with a 0.45 μm filter. Then, the filtrate was diluted to 0.1 mg/mL for circular dichroism.

Scheme 2. Synthesis of the Brushlike Selenopolypeptides and the Reversible Structure Changes upon Redox Reactions: (A) Structures and Nomenclature of the Brushlike Selenopolypeptides; DMPA, 2,2-dimethoxy-2-phenylacetophenone; and (B) Structural Changes during Redox Reactions
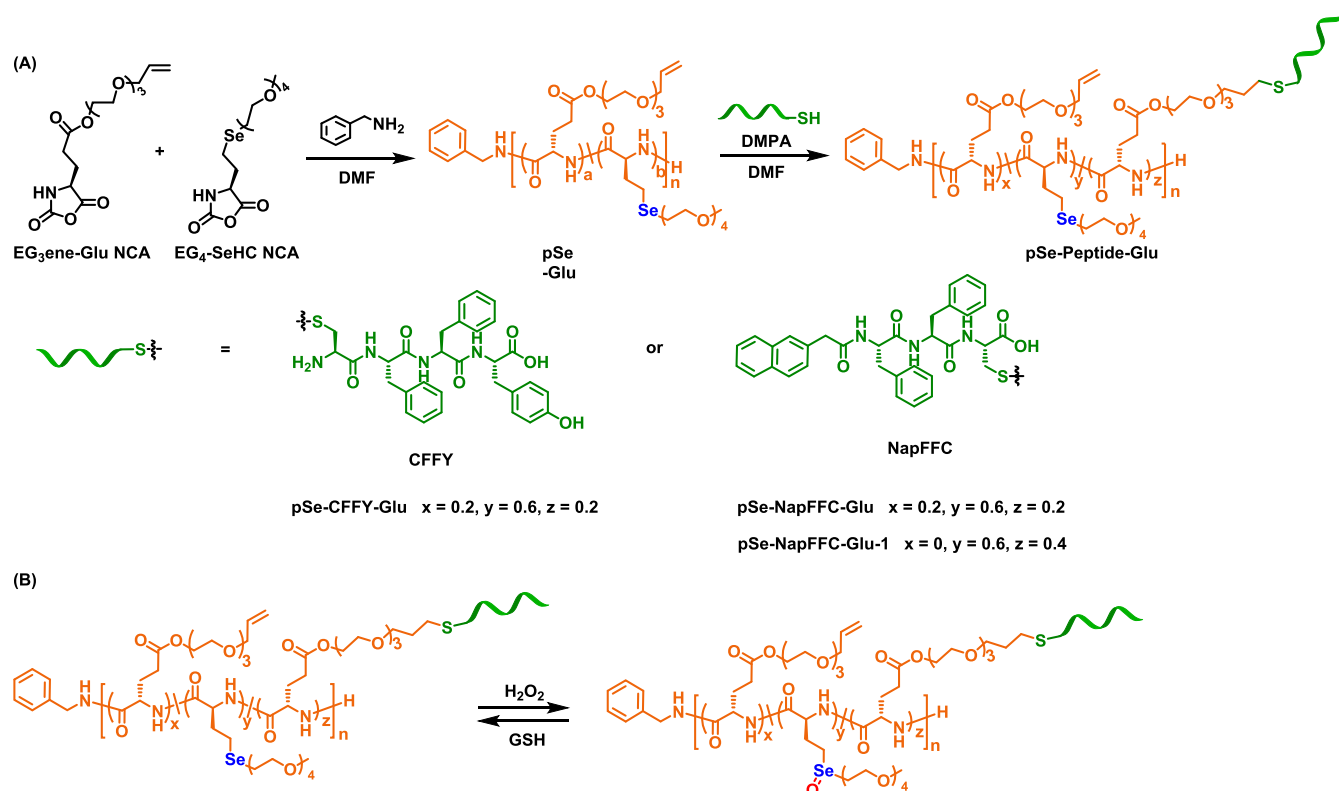
2.8. Circular Dichroism Spectroscopy.

Circular dichroism (CD) spectra were recorded using a sample concentration of 0.1 mg/mL in phosphate-buffered saline (PBS) (HT voltage, 215−593 V). Spectra were obtained from 260 to 190 nm with a 1.0 nm step, 1.0 nm bandwidth, and 1 s collection time per step at 37 °C in a 1 cm path length quartz cuvette.

2.9. Transmission Electron Microscopy (TEM).

TEM samples were examined using a LaB transmission electron microscope (Tecnai G2 20 S-TWIN) operating at 120 kV. The sample (10 μL, 5.0 mg/mL in PBS) was spotted onto 200 mesh carbon-coated copper grids and allowed to stand for 1 min. The excess sample was carefully removed by filter paper, and then, grids were immediately stained with uranyl acetate negative stain (10 μL for 1 min). Grids were allowed to air dry for 3 h. Dimensions of nanostructures were determined using ImageJ software.

2.10. Thioflavin T (ThT) Fluorescence Binding Assay.

Thioflavin T (ThT, 500 μM) in water was added to the conjugate solutions to obtain final concentrations of 50 μM ThT and 1.0−10.0 mg/mL polypeptide. The fluorescence intensity of the samples was recorded immediately at 37 °C. The fluorescence intensity was measured in 200 μL of samples in a 1 cm path length quartz cuvette. The samples were excited at 450 nm, and the fluorescence intensity was recorded at 490 nm using a 50 μM ThT solution in water as a blank.

2.11. Preparation of Nile Red-Loaded Micelles.

Polypeptide solution (in DMF) and Nile Red solution (in DMF) were mixed to obtain final concentrations of 5.0 mg/mL mixed solution. Then, 20 μL of mixed solution was added to 1 mL of water under vigorous stirring at room temperature. The mixture was centrifuged. The micelles were redispersed and filtered through a 0.45 μM pore-sized syringe filter.

2.12. Preparation and Characterization of Doxorubicin (Dox)-Loaded Micelles.

Doxorubicin hydrochloride (Dox·HCl) was dispersed in tetrahydrofuran (THF) in the presence of an excess amount of TEA under ultrasonic condition. The solution was added dropwise to an aqueous solution of selenopolypeptide (1.0 mg/mL) with stirring at a feed ratio of 30 wt %. Then, the solution was transferred into a dialysis bag (MWCO 3.5 kDa) and dialyzed against phosphate-buffered saline (PBS, pH 7.4) for 24 h with PBS changing every 3 h. Finally, the solution was centrifuged for 10 min at 5000 rpm and filtered through a 0.45 μm filter. Dox was determined by the absorption at 485 nm. The loading capacity of Dox was calculated according to the following equations

$$\text{loading capacity} = \text{weight of encapsulated Dox/weight of total Dox} \times 100\%$$

2.13. In Vitro Drug Release.

Upon the treatment of 97 mM H_2O_2, the cumulative release of the model compound (Nile Red) was determined by fitting the readout fluorescence at 620 nm (excitation at 570 nm). The percentage of Nile Red release was calculated according to the following equations:

$$\text{cumulative release of Nile Red} = 100\% - (\text{FI at 620 nm of different time/initial FI at 620 nm}) \times 100\%$$

2.14. Live Cell Imaging.

Cells were first placed in a glass chamber and then cultured with 2 mL of culture medium containing 1.0 mg/mL Nile Red-loaded micelles for 4 h. Then, the cells were rinsed with PBS at least five times. After the cell-containing glass chamber was fixed on the confocal microscope stage, fluorescent images were captured immediately.

2.15. Cell Viability.

HeLa cells and HcerEpic cells were cultured in a humidified CO$_2$ (5%) incubator at 37 °C in DMEM supplemented with 10% fetal bovine serum (FBS, Gibco) and 1% Pen Strep (PS, Gibco). Cell proliferation was assessed by the 3-(4,5-dimethylthiazol-2-yl)-2,5-diphenyltetrazolium bromide (MTT) assay. To measure the toxicity of empty polypeptide micelles against HeLa cells and HcerEpic cells, cells were incubated with 0.1−3.0 mg/mL of empty micelles for 24 h. To measure the cytotoxicity of Dox-loaded

micelles or free Dox, cells were incubated with 0.1−3.0 mg/mL of Dox-loaded micelles or free Dox for 24 h.

2.16. Tumor Inhibition Experiments. All animal studies were performed in accordance with the Institutional Animal Use and Care Regulations approved by the National Center for Nanoscience and Technology/Animal Care and Use Committee (NCNST/ACUC). The tumor-bearing mice model was established by subcutaneously injecting a suspension of 1×10^6 HeLa cells per mouse into the front flank of BALB/c nude mouse. When the tumor volume reached approximately 80−100 mm³, the mice were used for therapeutic studies. Mice in the treatment group received an intratumoral injection of 1.0 mg/kg or 5.0 mg/kg Dox-loaded micelles. Mice in the control groups received saline, 5.0 mg/kg empty micelles, or 5.0 mg/kg free Dox. Each group contains five mice. The mice received four treatments on days 1, 3, 5, and 7. The tumor size and body weight were measured every 2 days.

3. RESULTS AND DISCUSSION

3.1. Synthesis of Brushlike Selenopolypeptides. We began to synthesize the selenopolypeptide p(EG₄-SeHC)-*ran*-

Table 1. Secondary Structures of Brushlike Selenopolypeptides in the Reduced or Oxidized State

States	Brushlike selenopolypeptides		
	pSe-CFFY-Glu	pSe-NapFFC-Glu	pSe-NapFFC-Glu-1
native	α-helix[a]	α-helix	α-helix
oxidized	random coil[a]	β-sheet[a]	α-helix
reduced	α-helix	α-helix	n.d.[b]

[a]The secondary structure was determined by the CD signal.[52] The α-helical conformation showed negative peaks near 222 and 208 nm. The β-sheet conformation had a negative peak at 217−218 nm. The random coil conformation had a negative peak near 198 nm and a positive peak near 220 nm with low ellipticity. [b]pSe-NapFFC-Glu-1 had poor solubility in aqueous solution and was hard to be oxidized.

(EG₃ene-Glu) (abbreviated as pSe-Glu) through copolymerization of EG₄-SeHC NCA with EG₃ene-Glu NCA (Scheme 2 and Figure S5). The content of selenium and double bonds could be accurately controlled by the feeding ratio of different monomers as indicated by ¹H NMR (Figure S6). To ensure oxidation-induced secondary structure transition, the content of EG₃ene-Glu was optimized. We found that up to 40% EG₃ene-Glu could be introduced while the resulting selenopolypeptide retained efficient helix-to-coil transition upon oxidation. The cysteine-bearing peptide (CFFY or NapFFC) was then introduced to the selenopolypeptide through a thiol-ene reaction under UV irradiation to obtain pSe-peptide-Glu. The excessive short peptide was removed by dialysis in alkaline solutions, and the conjugates were recovered in quantitative yield under most of the cases. The grafting percentage was determined by ¹H NMR using the relative ratio between the methyl group on EG₄-SeHC and remaining double bonds (Figures S7 and S8).

Although FFY is a robust assembly tripeptide,[51] the assembling capacity of CFFY was unable to drive the assembly of selenopolypeptide pSe-CFFY-Glu (Table 1, Figures S9, and S10). Alternatively, NapFFC was a stronger assembly peptide that can form a self-supported hydrogel in PBS buffer (Figures S9, S11, and S12). Therefore, we conjugated NapFFC with polypeptide pSe-Glu to obtain two conjugates, namely, pSe-NapFFC-Glu (40% of the double bonds were modified) and pSe-NapFFC-Glu-1 (100% of the double bonds were modified). The fully modified polypeptide, pSe-NapFFC-Glu-1 was hard to be oxidized (Table 1 and Figure S13), presumably owing to the tight inter- and intra-molecular conjunction that hindered the access of the oxidant. In contrast, pSe-NapFFC-Glu could be readily oxidized in aqueous solutions upon oxidation of selenoether to selenoxide (Table 1, XPS analysis in Figure S14, and ¹H NMR analysis in
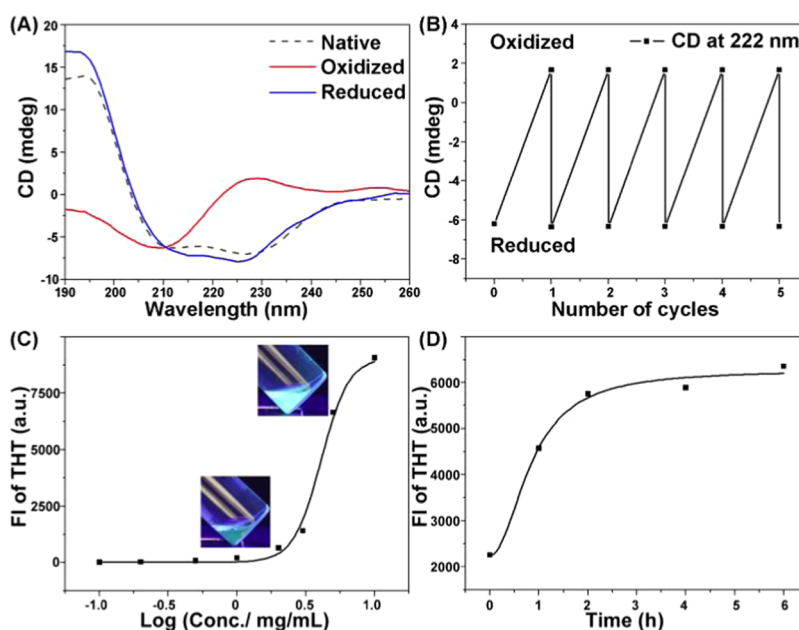

Figure 1. Secondary structure switch during the redox cycle. (A) CD spectra of pSe-NapFFC-Glu during redox reactions. Condition: 0.1 mg/mL pSe-NapFFC-Glu in PBS at pH 7.4. (B) Reversible conformation change of pSe-NapFFC-Glu indicated by the peak of 222 nm in CD spectra. (C) Fluorescent intensity of ThT depending on the concentration of oxidized pSe-NapFFC-Glu. (D) Time-dependent increase of ThT fluorescence during the oxidation of 5.0 mg/mL pSe-NapFFC-Glu in PBS at pH 7.4.
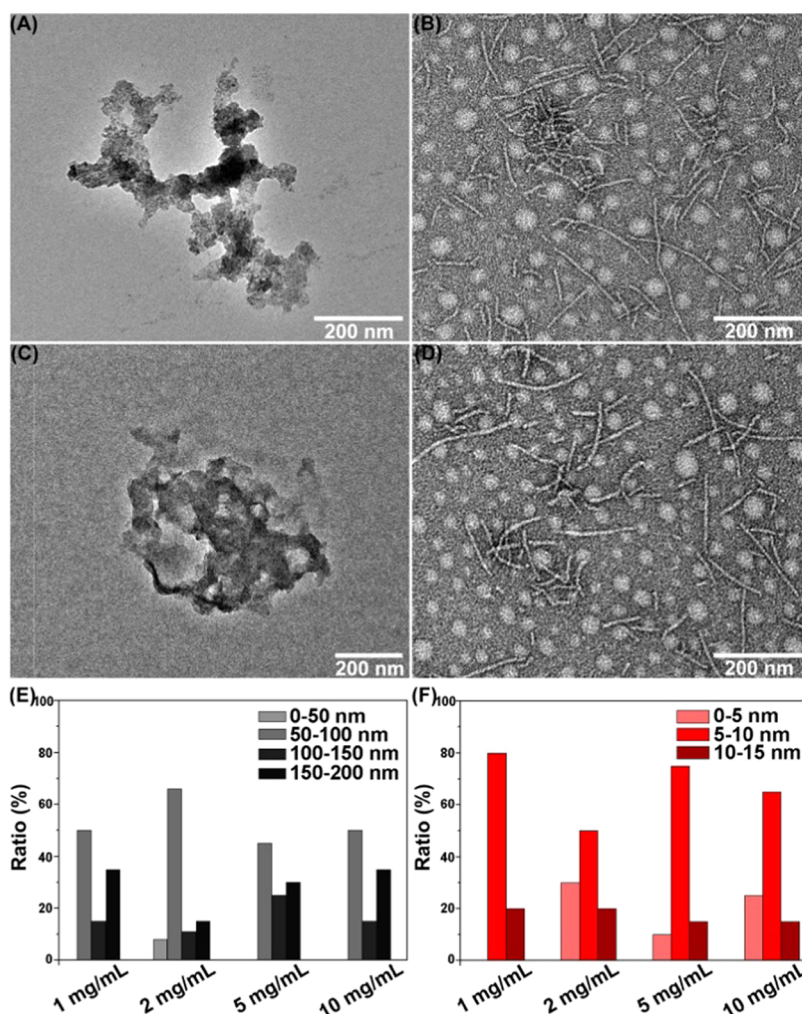
Figure 2. Morphology of pSe-NapFFC-Glu under different conditions. (A) Native condition, (B) oxidized condition, (C) reduced condition, and (D) re-oxidized condition. The concentration of H_2O_2 was 97 mM. (E) Statistics of nanofiber length versus concentration and (F) statistics of nanofiber width versus concentration.

Figure S15). Therefore, we chose pSe-NapFFC-Glu for further studies.

3.2. Redox-Regulated Conformation Switch and Self-Assembly. The overall conformation of the brushlike selenopolypeptide depended on the interplay between the structure of backbone pSe-Glu and appended short-peptide NapFFC. According to CD spectra, the as-prepared brushlike selenopolypeptide pSe-NapFFC-Glu mainly adopted the α-helix conformation. After oxidation, pSe-NapFFC-Glu adopted the β-sheet conformation with the characteristic negative band near 210 nm. The conversion from selenoether to selenoxide led to the helix-to-coil transition, which weakens the rigidity of the main chain. With a more flexible backbone, NapFFC could adopt the interchain β-sheet conformation and resulted in supramolecular assemblies. Different from sulfoxide, selenoxide could be readily reduced by thiol reductants such as glutathione (GSH).[50] Upon reduction, the α-helix conformation of the main chain can be restored (Figure 1A). More importantly, this redox-driven conformation switch was fully reversible for at least five cycles. According to the sequential CD spectra (Figure S16) or the value at 222 nm (Figure 1B), the attenuation of α-helix in the backbone accompanied with the emergence of β-sheet among the branches, vice versa.

The formation of β-sheet was further verified by β-sheet indicator ThT.[53] The emission intensity of ThT was dependent on the concentration of oxidized pSe-NapFFC-Glu. In a steady setup, there was a sharp increase of the ThT emission when the concentration of oxidized pSe-NapFFC-Glu exceeded 1.0 mg/mL (Figure 1C). While in a dynamic setup in which ThT was initially mixed with reduced pSe-NapFFC-Glu, the emission increased after the addition of an oxidant (e.g., H_2O_2) and reached a plateau at 6 h (Figure 1D). Both results confirmed that oxidized pSe-NapFFC-Glu would form a β-sheet structure.

The secondary conformation switch could tune the micromorphology of pSe-NapFFC-Glu. As shown in Figure 2A, native pSe-NapFFC-Glu formed relatively large aggregates (though can be converted to micelles after micellization). Upon oxidation, plenty of nanofibers was generated (Figure 2B). Then, it can be restored to the amorphous aggregates after reduction and nanofibers after oxidation repeatedly, in good agreement with the conformation switch (Figure 2C,D). According to the statistics (Figure 2E,F), the nanofibers owned a length distribution ranging 50−200 nm and width distribution ranging 5−15 nm. Interestingly, the major species fell in the dimension of 50−100 nm in length and 5−10 nm in
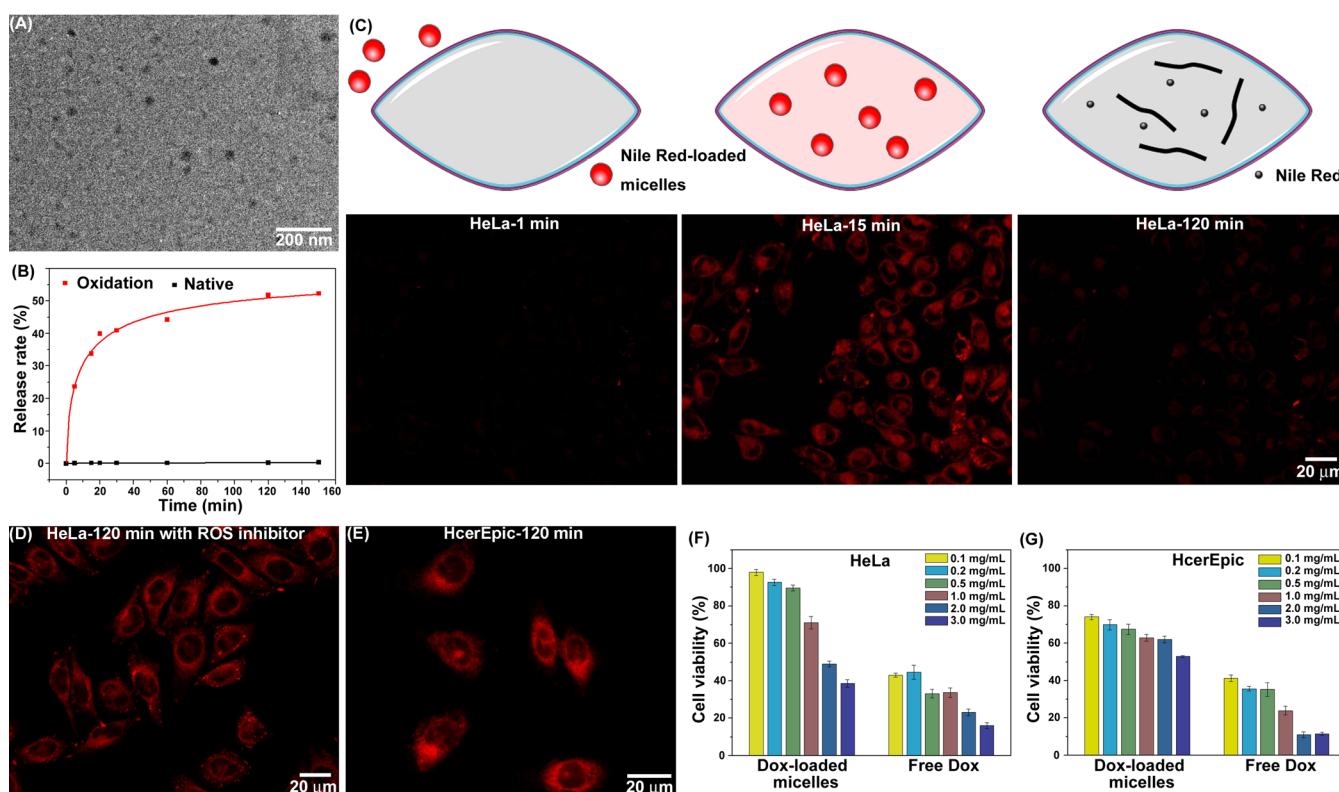
Figure 3. Responsive drug delivery inside live cells. (A) TEM image of Nile Red-loaded micelles. (B) Cumulative release of Nile Red from Nile Red-loaded micelles upon oxidation. Confocal laser scanning microscope (CLSM) images of (C) HeLa cells cultured with Nile Red-loaded micelles after a certain incubation time (1, 15, and 120 min), (D) HeLa cells pre-treated with a reactive oxygen species (ROS) inhibitor for 30 min and then incubated with Nile Red-loaded micelles for 120 min and (E) HcerEpic cells incubated with Nile Red-loaded micelles for 120 min. Cytotoxicity of Dox-loaded micelles against (F) HeLa cells and (G) HcerEpic cells. HeLa cells or HcerEpic cells were incubated with gradient concentrations of Dox-loaded micelles for 24 h.

width, which was independent of concentrations and thus should be related to the intrinsic polypeptide components.

3.3. Responsive Drug Delivery Inside Live Cells. Amphiphilic brushlike selenopolypeptide pSe-NapFFC-Glu can be formulated into micelles in aqueous solutions for controlled drug release. Nile Red was chosen as a model molecule to study the redox-regulated release behavior of drug-loaded micelles. Figure 3A shows the morphology of the as-prepared Nile Red-loaded micelles (pSe-NapFFC-Glu/Nile Red = 50:1 w/w). The size of the micelles was 26.0 ± 3.1 nm on average. Micelle-capsulated Nile Red gave strong red fluorescence.[54] Upon Nile Red release from the micelles into an aqueous environment, the fluorescence intensity of Nile Red would significantly decrease. By measuring the remaining fluorescence intensity, we can calculate the cumulative release profile of Nile Red from the micelles in a time-dependent manner. Results showed that oxidization could trigger around 50% release of Nile Red from micelles, while the native micelle itself barely released Nile Red (Figure 3B). The accelerated release of cargo after oxidation should be attributed to the increase of β-sheets in nanofibers than in micelles.[55]

Cellular uptake of Nile Red-loaded micelles was monitored using CLSM. As shown in Figure 3C, there was negligible fluorescence of Nile Red in HeLa cells after incubation with Nile Red-loaded micelles for 1 min. The fluorescence increased significantly in HeLa cells within the following 15 min and then diminished after 120 min incubation. The increase of fluorescence from 1 to 15 min should be ascribed to the gradual endocytosis and accumulation of Nile Red-loaded

micelles inside HeLa cells. In contrast, the subsequent decrease of emission may be due to the release of Nile Red from micelles upon oxidation by a high level of intracellular ROS. Accordingly, by fragmenting the HeLa cells preincubated with Nile Red-loaded micelles for 15 min and 120 min, we found micelles and nanofibers, respectively (Figure S17). Another group of HeLa cells pretreated with an ROS inhibitor and then incubated with Nile Red-loaded micelles showed strong fluorescence after 120 min without oxidation (Figure 3D). TEM of cell fragment showed micelles in HeLa cells with pretreatment of the ROS inhibitor (Figure S18). Analytical high-performance liquid chromatography (HPLC) further demonstrated that after 120 min incubation, the total concentration of Nile Red molecules retained inside HeLa cells with or without ROS inhibitor treatment was similar, although the emission differed drastically (Figure 3C right panel, three-dimensional (3D) and Figure S19). These results indicated that Nile Red-loaded micelles could enter live HeLa cells and then transform to nanofibers upon ROS-mediated oxidation to release cargoes. While in normal HcerEpic cells with low levels of ROS, strong red fluorescence emission was still observed after incubation for 120 min, indicating a large portion of intact Nile Red-loaded micelles (Figure 3E). Taking together, the cargo-loaded micelles could selectively release cargoes in cancer cells rather than normal cells.

Furthermore, typical chemotherapeutic agent doxorubicin (Dox) was encapsulated into the selenopolypeptide micelles with a loading capacity of 16.7%. Before studying the intracellular Dox release from Dox-loaded micelles, we first
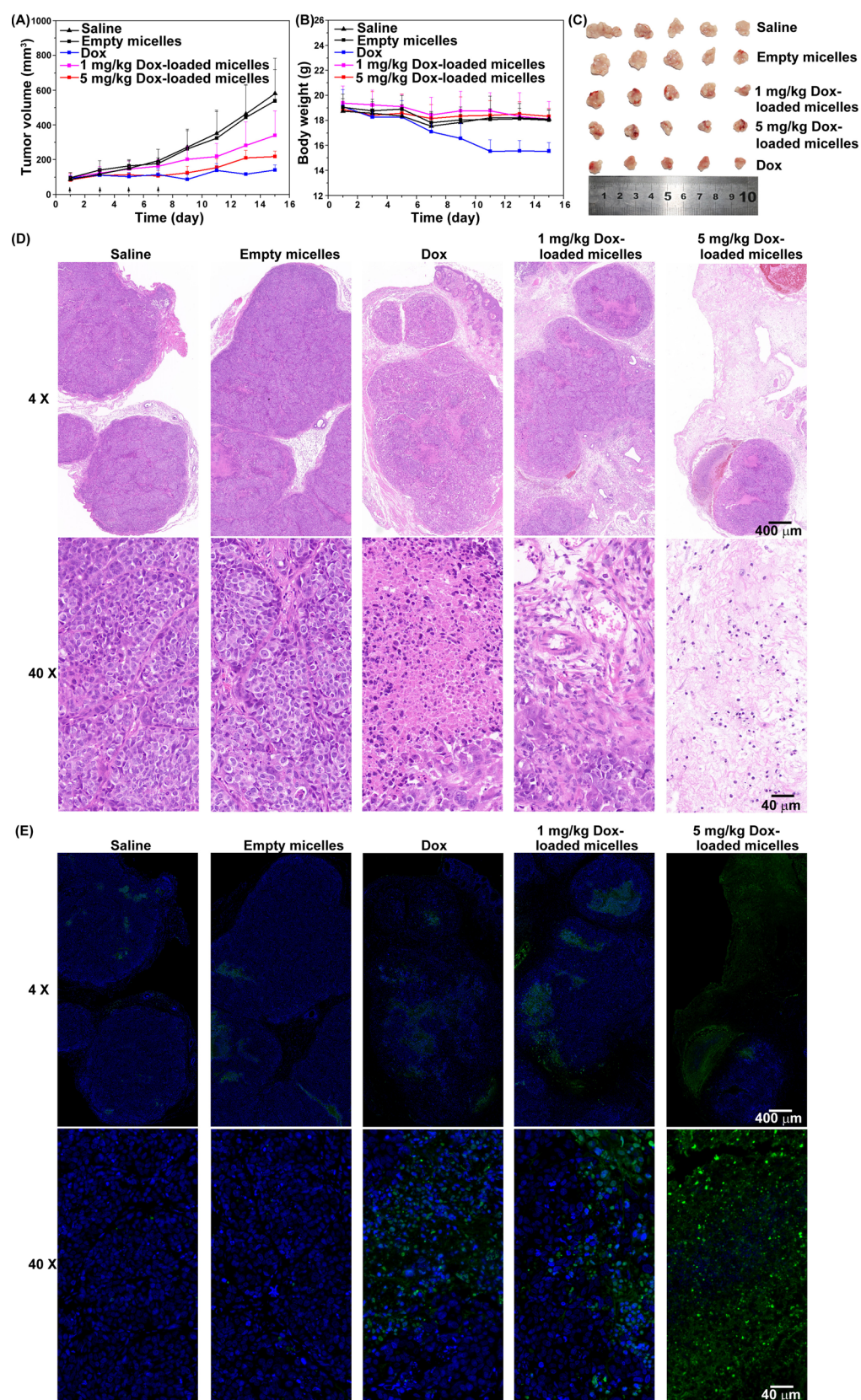
Figure 4. *In vivo* anticancer efficacy of Dox-loaded micelles. (A) Tumor growth curves for mice after intratumoral injection with saline, empty micelles, 5.0 mg/kg free Dox, 1.0 mg/kg Dox-loaded micelles, and 5.0 mg/kg Dox-loaded micelles ($n = 5$). The arrows on the *x*-axis indicated treatment duration in days. (B) Average mouse weights in each group. (C) Optical images of dissected tumor samples after treatment for 14 days. (D) Representative histological examination results of the dissected tumors using haematoxylin−eosin (HE) staining. (E) Terminal deoxynucleotidyl transferase-mediated dUTP nick end labeling (TUNEL) assays (green fluorescence) of the dissected HeLa tumors after the treatment.

incubated HeLa cells and HcerEpic cells with empty micelles to verify the biocompatibility of the vehicles. Based on a standard MTT assay, the viability of both HeLa cells and HcerEpic cells remained >75% after incubation with 3.0 mg/mL empty micelles for 24 h (Figure S20), indicating that empty micelles were biocompatible as a drug delivery vehicle. Then, the cytotoxicity of Dox-loaded micelles against HeLa cells and HcerEpic cells was studied. The viability of HeLa cells after incubation with Dox-loaded micelles was significantly decreased in a concentration-dependent manner (Figure 3F). As the overall cytotoxicity was slightly weaker than the free Dox, this result implied the capable release of Dox from micelles in HeLa cells albeit a partial release as indicated by the release profile of Nile Red (Figure 3B). While in HcerEpic cells, which were more sensitive to free Dox, the Dox-loaded micelles could alleviate cytotoxicity than the equivalent amount of free Dox (Figure 3G), implying a certain portion of retained Dox inside micelles.

3.4. *In Vivo* Anticancer Efficacy. Taking into account the conformation and morphology transitions of selenopolypeptide in response to ROS, we further explored their potential applications in anticancer treatment. To investigate the therapeutic potential of Dox-loaded micelles, we randomly allocated HeLa tumor-bearing BALB/c nude mice into five groups ($n = 5$) and treated each group through intratumor injection as follows: saline, empty micelles, free Dox, and Dox-loaded micelles with varied dose. Injections were carried out four times at intervals of 2 d. Mice treated with saline, empty micelles, and 1.0 mg/kg of Dox-loaded micelles formed fast-growing tumors (Figure 4A). In contrast, tumor growth was markedly inhibited by the 5.0 mg/kg Dox-loaded micelles. For the group that received free Dox, although tumor growth could be inhibited with 5.0 mg/kg Dox, the body weight decreased substantially (Figure 4B), owing to the systemic toxicity of Dox. In contrast, the body weights of mice in the 5.0 mg/kg Dox-loaded micelles treatment group remained steady after treatment, indicating satisfactory biosafety.

After 14-day treatment, the mice were sacrificed and tumors were dissected (Figure 4C) for histological examination with haematoxylin−eosin (HE) staining. As shown in Figure 4D, more necrotic regions of the tumors were observed in the 5.0 mg/kg Dox-loaded micelles treatment group, exhibiting cell shrinkage, loss of contact, and coagulation, which was similar to the tumors treated with free Dox. These observations indicated that tumor cells can be efficiently destroyed by released Dox. However, tumors treated with 1.0 mg/kg Dox-loaded micelles exhibited less necrotic region and the tumors treated with saline or free micelles demonstrated that the HeLa cells remained normal. We further conducted the terminal deoxynucleotidyl transferase-mediated dUTP nick end labeling (TUNEL) assay to validate the tumor apoptosis after treatment. According to Figure 4E, most cells in tumor tissue in the treatment group were TUNEL positive, indicative of DNA fragmentation. To further determine possible systemic toxicity, the major organs were harvested for histological analysis as well. The group receiving Dox-loaded micelles did not exhibit any observable differences compared to the saline control group based on the histological examination of the heart, liver, spleen, lungs, and kidneys (Figure S21), which further indicated the excellent biocompatibility and safety of our strategy.

4. CONCLUSIONS

In summary, we reported the redox-driven reversible supramolecular assemblies via switching the conformation of brushlike selenopolypeptides. Our system studied the interplay (e.g., competition and balance) between two typical peptide secondary structures (α-helix and β-sheet) to realize the dynamic self-assembly process with controlled nanomorphology in correspondence. The properties of selenopolypeptide with conformation and morphology transitions can be further utilized as the delivery vehicles to realize drug-controlled release, demonstrating the potential applications in anticancer therapeutics. While in an open system such as live cells or animals, the assembling components may diffuse away, leaving the reversible transformation (nanofibers to micelles) to be further elucidated. Overall, the exploration of such a biochemical reaction (e.g., redox)-driven reversible self-assembly system should facilitate the development of adaptive bionanomaterials.

■ ASSOCIATED CONTENT

Ⓢ Supporting Information

The Supporting Information is available free of charge at https://pubs.acs.org/doi/10.1021/acs.biomac.1c00300.

> Synthesis and characterization of the brushlike selenopolypeptide and histology and biocompatibility analysis of the brushlike selenopolypeptide (PDF)

■ AUTHOR INFORMATION

Corresponding Authors

Hua Lu − *Beijing National Laboratory for Molecular Sciences Center for Soft Matter Science and Engineering, Key Laboratory of Polymer Chemistry and Physics of Ministry of Education, College of Chemistry and Molecular Engineering, Peking University, Beijing 100871, P. R. China;* ⓞ orcid.org/0000-0003-2180-3091; Email: chemhualu@pku.edu.cn

Yuan Gao − *CAS Center of Excellence for Nanoscience, Key Laboratory of Biomedical Effects of Nanomaterials and Nanosafety, Chinese Academy of Sciences, National Center for Nanoscience and Technology, Beijing 100190, P. R. China; University of Chinese Academy of Sciences, Beijing 100049, P. R. China;* ⓞ orcid.org/0000-0001-9714-4219; Email: gaoy@nanoctr.cn

Authors

Qingxin Yao − *CAS Center of Excellence for Nanoscience, Key Laboratory of Biomedical Effects of Nanomaterials and Nanosafety, Chinese Academy of Sciences, National Center for Nanoscience and Technology, Beijing 100190, P. R. China; University of Chinese Academy of Sciences, Beijing 100049, P. R. China*

Guangqi Wu − *Beijing National Laboratory for Molecular Sciences Center for Soft Matter Science and Engineering, Key Laboratory of Polymer Chemistry and Physics of Ministry of Education, College of Chemistry and Molecular Engineering, Peking University, Beijing 100871, P. R. China;* ⓞ orcid.org/0000-0002-9763-6982

Hao Hao − *CAS Center of Excellence for Nanoscience, Key Laboratory of Biomedical Effects of Nanomaterials and Nanosafety, Chinese Academy of Sciences, National Center for Nanoscience and Technology, Beijing 100190, P. R. China*

Complete contact information is available at:

https://pubs.acs.org/10.1021/acs.biomac.1c00300

Author Contributions

‖Q.Y., G.W., and H.H. contributed equally to this work.

Notes

The authors declare no competing financial interest.

■ REFERENCES

(1) Dixon, J. R.; Selvaraj, S.; Yue, F.; Kim, A.; Li, Y.; Shen, Y.; Hu, M.; Liu, J. S.; Ren, B. Topological domains in mammalian genomes identified by analysis of chromatin interactions. *Nature* **2012**, *485*, 376−380.

(2) Wang, S. Y.; Su, J. H.; Beliveau, B. J.; Bintu, B.; Moffitt, J. R.; Wu, C. T.; Zhuang, X. W. Spatial organization of chromatin domains and compartments in single chromosomes. *Science* **2016**, *353*, 598−602.

(3) Fletcher, D. A.; Mullins, D. Cell mechanics and the cytoskeleton. *Nature* **2010**, *463*, 485−492.

(4) Pollard, T. D.; Cooper, J. A. Actin, a Central Player in Cell Shape and Movement. *Science* **2009**, *326*, 1208−1212.

(5) He, H.; Tan, W.; Guo, J.; Yi, M.; Shy, A. N.; Xu, B. Enzymatic Noncovalent Synthesis. *Chem. Rev.* **2020**, *120*, 9994−10078.

(6) Wang, H. M.; Feng, Z. Q. Q.; Xu, B. Bioinspired assembly of small molecules in cell milieu. *Chem. Soc. Rev.* **2017**, *46*, 2421−2436.

(7) Cao, W.; Zhang, X.; Miao, X.; Yang, Z.; Xu, H. gamma-Ray-responsive supramolecular hydrogel based on a diselenide-containing polymer and a peptide. *Angew. Chem., Int. Ed.* **2013**, *52*, 6233−6237.

(8) Shi, W.; Huang, J.; Fang, R.; Liu, M. Imparting Functionality to the Hydrogel by Magnetic-Field-Induced Nano-assembly and Macro-response. *ACS Appl. Mater. Interfaces* **2020**, *12*, 5177−5194.

(9) Guo, X.; Su, J.; Guo, H. Electric field induced orientation and self-assembly of carbon nanotubes in water. *Soft Matter* **2012**, *8*, 1010−1016.

(10) You, Y. Z.; Yan, J. J.; Yu, Z. Q.; Cui, M. M.; Hong, C. Y.; Qu, B. J. Multi-responsive carbon nanotube gel prepared via ultrasound-induced assembly. *J. Mater. Chem.* **2009**, *19*, 7656−7660.

(11) Holten-Andersen, N.; Harrington, M. J.; Birkedal, H.; Lee, B. P.; Messersmith, P. B.; Lee, K. Y. C.; Waite, J. H. pH-induced metal-ligand cross-links inspired by mussel yield self-healing polymer networks with near-covalent elastic moduli. *Proc. Natl. Acad. Sci. U.S.A.* **2011**, *108*, 2651−2655.

(12) Gong, N.; Zhang, Y.; Teng, X.; Wang, Y.; Huo, S.; Qing, G.; Ni, Q.; Li, X.; Wang, J.; Ye, X.; Zhang, T.; Chen, S.; Wang, Y.; Yu, J.; Wang, P. C.; Gan, Y.; Zhang, J.; Mitchell, M. J.; Li, J.; Liang, X. J. Proton-driven transformable nanovaccine for cancer immunotherapy. *Nat. Nanotechnol.* **2020**, *15*, 1053−1064.

(13) Aujard-Catot, J.; Nguyen, M.; Bijani, C.; Pratviel, G.; Bonduelle, C. Cd^{2+} coordination: an efficient structuring switch for polypeptide polymers. *Polym. Chem.* **2018**, *9*, 4100−4107.

(14) Felip-León, C.; Galindo, F.; Miravet, J. F.; Castelletto, V.; Hamley, I. W. Thermally Regulated Reversible Formation of Vesicle-Like Assemblies by Hexaproline Amphiphiles. *J. Phys. Chem. B* **2017**, *121*, 7443−7446.

(15) Yan, Q.; Zhao, Y. CO2-Stimulated Diversiform Deformations of Polymer Assemblies. *J. Am. Chem. Soc.* **2013**, *135*, 16300−16303.

(16) Huang, Z. T.; Yao, Q. X.; Chen, J. L.; Gao, Y. Redox supramolecular self-assemblies nonlinearly enhance fluorescence to identify cancer cells. *Chem. Commun.* **2018**, *54*, 5385−5388.

(17) Nguyen, M.; Stigliani, J. L.; Pratviel, G.; Bonduelle, C. Nucleopolypeptides with DNA-triggered alpha helix-to-beta sheet transition. *Chem. Commun.* **2017**, *53*, 7501−7504.

(18) Nguyen, M.; Stigliani, J. L.; Bijani, C.; Verhaeghe, P.; Pratviel, G.; Bonduelle, C. Ionic Polypeptide Polymers with Unusual beta-Sheet Stability. *Biomacromolecules* **2018**, *19*, 4068−4074.

(19) Mazo, A. R.; Allison-Logan, S.; Karimi, F.; Chan, N. J. A.; Qiu, W. L.; Duan, W.; O'Brien-Simpson, N. M.; Qiao, G. G. Ring opening polymerization of alpha-amino acids: advances in synthesis, architecture and applications of polypeptides and their hybrids. *Chem. Soc. Rev.* **2020**, *49*, 4737−4834.

(20) Song, Z. Y.; Han, Z. Y.; Lv, S. X.; Chen, C. Y.; Chen, L.; Yin, L. C.; Cheng, J. J. Synthetic polypeptides: from polymer design to supramolecular assembly and biomedical application. *Chem. Soc. Rev.* **2017**, *46*, 6570−6599.

(21) Song, Z. Y.; Tan, Z. Z.; Cheng, J. J. Recent Advances and Future Perspectives of Synthetic Polypeptides from N-Carboxyanhydrides. *Macromolecules* **2019**, *52*, 8521−8539.

(22) Song, Z. Y.; Fu, H. L.; Wang, R.; Pacheco, L. A.; Wang, X.; Lin, Y.; Cheng, J. J. Secondary structures in synthetic polypeptides from N-carboxyanhydrides: design, modulation, association, and material applications. *Chem. Soc. Rev.* **2018**, *47*, 7401−7425.

(23) Nowak, A. P.; Breedveld, V.; Pakstis, L.; Ozbas, B.; Pine, D. J.; Pochan, D.; Deming, T. J. Rapidly recovering hydrogel scaffolds from self-assembling diblock copolypeptide amphiphiles. *Nature* **2002**, *417*, 424−428.

(24) Huang, J.; Heise, A. Stimuli responsive synthetic polypeptides derived from *N*-carboxyanhydride (NCA) polymerisation. *Chem. Soc. Rev.* **2013**, *42*, 7373−7390.

(25) Yuan, J. S.; Zhang, Y.; Sun, Y.; Cai, Z. C.; Yang, L. J.; Lu, H. Salt- and pH-Triggered Helix-Coil Transition of Ionic Polypeptides under Physiology Conditions. *Biomacromolecules* **2018**, *19*, 2089−2097.

(26) Xiong, W.; Fu, X. H.; Wan, Y. M.; Sun, Y. L.; Li, Z. B.; Lu, H. Synthesis and multimodal responsiveness of poly(alpha-amino acid)s bearing OEGylated azobenzene side-chains. *Polym. Chem.* **2016**, *7*, 6375−6382.

(27) Kramer, J. R.; Deming, T. J. Multimodal Switching of Conformation and Solubility in Homocysteine Derived Polypeptides. *J. Am. Chem. Soc.* **2014**, *136*, 5547−5550.

(28) Fu, X. H.; Ma, Y. A.; Shen, Y.; Fu, W. X.; Li, Z. B. Oxidation-Responsive OEGylated Poly-L-cysteine and Solution Properties Studies. *Biomacromolecules* **2014**, *15*, 1055−1061.

(29) Ma, Y. N.; Fu, X. H.; Shen, Y.; Fu, W. X.; Li, Z. B. Irreversible Low Critical Solution Temperature Behaviors of Thermal-responsive OEGylated Poly(L-cysteine) Containing Disulfide Bonds. *Macromolecules* **2014**, *47*, 4684−4689.

(30) Chen, C. Y.; Wang, Z. H.; Li, Z. B. Thermoresponsive Polypeptides from Pegylated Poly-L-glutamates. *Biomacromolecules* **2011**, *12*, 2859−2863.

(31) Wang, S.; He, W.; Xiao, C.; Tao, Y.; Wang, X. Synthesis of Y-Shaped OEGylated Poly(amino acid)s: The Impact of OEG Architecture. *Biomacromolecules* **2019**, *20*, 1655−1666.

(32) Ulijn, R. V.; Smith, A. M. Designing peptide based nanomaterials. *Chem. Soc. Rev.* **2008**, *37*, 664−675.

(33) Zhang, S. G. Fabrication of novel biomaterials through molecular self-assembly. *Nat. Biotechnol.* **2003**, *21*, 1171−1178.

(34) Mart, R. J.; Osborne, R. D.; Stevens, M. M.; Ulijn, R. V. Peptide-based stimuli-responsive biomaterials. *Soft Matter* **2006**, *2*, 822−835.

(35) Aggeli, A.; Bell, M.; Boden, N.; Keen, J. N.; Knowles, P. F.; McLeish, T. C. B.; Pitkeathly, M.; Radford, S. E. Responsive gels formed by the spontaneous self-assembly of peptides into polymeric beta-sheet tapes. *Nature* **1997**, *386*, 259−262.

(36) Li, J.; Du, X. W.; Hashim, S.; Shy, A.; Xu, B. Aromatic-Aromatic Interactions Enable alpha-Helix to beta-Sheet Transition of Peptides to Form Supramolecular Hydrogels. *J. Am. Chem. Soc.* **2017**, *139*, 71–74.

(37) Deng, C.; Wu, J. T.; Cheng, R.; Meng, F. H.; Klok, H. A.; Zhong, Z. Y. Functional polypeptide and hybrid materials: Precision synthesis via alpha-amino acid *N*-carboxyanhydride polymerization and emerging biomedical applications. *Prog. Polym. Sci.* **2014**, *39*, 330–364.

(38) Zhou, X. F.; Li, Z. B. Advances and Biomedical Applications of Polypeptide Hydrogels Derived from alpha-Amino Acid *N*-Carboxyanhydride (NCA) Polymerizations. *Adv. Healthcare Mater.* **2018**, *7*, No. e1800020.

(39) Deming, T. J. Functional Modification of Thioether Groups in Peptides, Polypeptides, and Proteins. *Bioconjugate Chem.* **2017**, *28*, 691–700.

(40) Kramer, J. R.; Deming, T. J. Glycopolypeptides with a Redox-Triggered Helix-to-Coil Transition. *J. Am. Chem. Soc.* **2012**, *134*, 4112–4115.

(41) Gharakhanian, E. G.; Bahrun, E.; Deming, T. J. Influence of Sulfoxide Group Placement on Polypeptide Conformational Stability. *J. Am. Chem. Soc.* **2019**, *141*, 14530–14533.

(42) Liu, H.; Wang, R.; Wei, J.; Cheng, C.; Zheng, Y.; Pan, Y.; He, X. L.; Ding, M. M.; Tan, H.; Fu, Q. Conformation-Directed Micelle-to-Vesicle Transition of Cholesterol Decorated Polypeptide Triggered by Oxidation. *J. Am. Chem. Soc.* **2018**, *140*, 6604–6610.

(43) Xu, Q. H.; He, C. L.; Ren, K. X.; Xiao, C. S.; Chen, X. S. Thermosensitive Polypeptide Hydrogels as a Platform for ROS-Triggered Cargo Release with Innate Cytoprotective Ability under Oxidative Stress. *Adv. Healthcare Mater.* **2016**, *5*, 1979–1990.

(44) Yu, S. J.; Wang, C.; Yu, J. C.; Wang, J. Q.; Lu, Y.; Zhang, Y. Q.; Zhang, X. D.; Hu, Q. Y.; Sun, W. J.; He, C. L.; Chen, X. S.; Gu, Z. Injectable Bioresponsive Gel Depot for Enhanced Immune Checkpoint Blockade. *Adv. Mater.* **2018**, *30*, No. e1801527.

(45) Rodriguez, A. R.; Kramer, J. R.; Deming, T. J. Enzyme-Triggered Cargo Release from Methionine Sulfoxide Containing Copolypeptide Vesicles. *Biomacromolecules* **2013**, *14*, 3610–3614.

(46) Xu, H. P.; Cao, W.; Zhang, X. Selenium-Containing Polymers: Promising Biomaterials for Controlled Release and Enzyme Mimics. *Acc. Chem. Res.* **2013**, *46*, 1647–1658.

(47) Xia, J. H.; Li, T. Y.; Lu, C. J.; Xu, H. P. Selenium-Containing Polymers: Perspectives toward Diverse Applications in Both Adaptive and Biomedical Materials. *Macromolecules* **2018**, *51*, 7435–7455.

(48) Li, Q. L.; Zhang, Y. Y.; Chen, Z. J.; Pan, X. Q.; Zhang, Z. B.; Zhu, J.; Zhu, X. L. Organoselenium chemistry-based polymer synthesis. *Org. Chem. Front.* **2020**, *7*, 2815–2841.

(49) Huang, Z. P.; Luo, Q.; Guan, S. W.; Gao, J. X.; Wang, Y. G.; Zhang, B.; Wang, L.; Xu, J. Y.; Dong, Z. Y.; Liu, J. Q. Redox control of GPx catalytic activity through mediating self-assembly of Fmoc-phenylalanine selenide into switchable supramolecular architectures. *Soft Matter* **2014**, *10*, 9695–9701.

(50) Wu, G. Q.; Ge, C. L.; Liu, X. Y.; Wang, S.; Wang, L. T.; Yin, L. C.; Lu, H. Synthesis of water soluble and multi-responsive selenopolypeptides via ring-opening polymerization of *N*-carboxyanhydrides. *Chem. Commun.* **2019**, *55*, 7860–7863.

(51) Frederix, P. W. J. M.; Scott, G. G.; Abul-Haija, Y. M.; Kalafatovic, D.; Pappas, C. G.; Javid, N.; Hunt, N. T.; Ulijn, R. V.; Tuttle, T. Exploring the sequence space for (tri-) peptide self-assembly to design and discover. *Nat. Chem.* **2015**, *7*, 30–37.

(52) Greenfield, N. J. Using circular dichroism spectra to estimate protein secondary structure. *Nat. Protoc.* **2006**, *1*, 2876–90.

(53) Krebs, M. R. H.; Bromley, E. H. C.; Donald, A. M. The binding of thioflavin-T to amyloid fibrils: localisation and implications. *J. Struct. Biol.* **2005**, *149*, 30–37.

(54) Jin, S.; Jeena, M. T.; Jana, B.; Moon, M.; Choi, H.; Lee, E.; Ryu, J. H. Spatiotemporal Self-Assembly of Peptides Dictates Cancer-Selective Toxicity. *Biomacromolecules* **2020**, *21*, 4806–4813.

(55) Wei, Q. N.; Huang, A. M.; Ma, L.; Huang, Z. L.; Huang, X.; Qiang, P. P.; Gong, Z. P.; Zhang, L. Structure regulation of silk fibroin films for controlled drug release. *J. Appl. Polym. Sci.* **2012**, *125*, E477–E484.